Nanoscale

REVIEW

View Article Online
View Journal | View Issue

Cite this: *Nanoscale*, 2017, **9**, 19001

In situ/*operando* characterization techniques for rechargeable lithium–sulfur batteries: a review

Jian Tan,[a] Dongna Liu,[a] Xu Xu*[a] and Liqiang Mai *[a,b]

Received 13th September 2017,
Accepted 15th November 2017

DOI: 10.1039/c7nr06819k

rsc.li/nanoscale

Rechargeable lithium–sulfur (Li–S) batteries have recently attracted global research interest due to their high theoretical specific capacity and energy density. To improve the performance and cycling stability of Li–S batteries, a clear understanding of the electrochemical reaction process and the degradation mechanisms of the sulfur redox chemistry are extremely important. In the past few decades, various advanced *in situ*/*operando* characterization tools have emerged, which have facilitated the understanding of the degradation mechanisms and the further development of high-performance Li–S batteries. In this review, we have summarized recent significant advances in *in situ*/*operando* characterization techniques for Li–S batteries. In particular, because of the existence of the soluble polysulfide species during the charge/discharge process, many creative ideas have been introduced into *in situ*/*operando* characterization of the electrochemical process in Li–S batteries.

1. Introduction

1.1. Overview of Li–S batteries

To satisfy the continuously ever-increasing energy demands of modern society, an increasing number of green, economic, and efficient energy storage systems have been explored.[1–11] Among these, Li–S batteries are regarded as one of the most promising candidates for the next-generation rechargeable batteries owing to their high theoretical specific capacity (1675 mA h g^{-1}, based on the complete conversion of S to Li_2S) and thus high theoretical energy density (2600 W h kg^{-1}), which is 3–5 times higher than that of the current state-of-the-art commercial lithium-ion batteries (LIBs).[12–15] Additionally, sulfur is one of the most abundant elements on earth, which is inexpensive, nontoxic, and environmentally friendly.[16–24] Despite these appealing advantages, the previously reported electrochemical performance of Li–S batteries is less satisfied as compared to the expectations, especially the poor cycling stability caused by the low Coulombic efficiency, the dissolution and undesirable diffusion of polysulfides, and the huge volumetric expansion during the charge/discharge process.[25–33]

To overcome these considerable challenges of Li–S batteries, we need to have a basic understanding of the charge/discharge reaction mechanism. During the discharge process, the lithium metal is oxidized at the lithium anode (negative electrode) to form lithium ions and electrons. The lithium ions travel to reach the sulfur cathode (positive electrode) *via* the electrolyte, whereas the electrons move to the positive electrode through the external circuit (eqn (1)). At the positive electrode, where sulfur reacts with the lithium ions and electrons to form lithium sulfide (Li_2S) (eqn (2)), while the opposite reactions will occur during the charge process at the negative electrode (eqn (3) and (4)), and the reaction of the total electrochemical process is presented (eqn (5)), as shown in Fig. 1a.

Lithiation (discharge) process:

Negative electrode: oxidation reaction (losing electrons)

$$Li \rightarrow Li^+ + e^- \quad (1)$$

Positive electrode: reduction reaction (gaining electrons)

$$S_8 + 16Li^+ + 16e^- \rightarrow 8Li_2S \quad (2)$$

Delithiation (charge) process:

Positive electrode: oxidation reaction (losing electrons)

$$8Li_2S \rightarrow S_8 + 16Li^+ + 16e^- \quad (3)$$

Negative electrode: reduction reaction (gaining electrons)

$$Li^+ + e^- \rightarrow Li \quad (4)$$

The overall electrochemical reaction:

$$S_8 + 16Li \rightarrow 8Li_2S \quad (5)$$

Typically, an ideal discharge curve consists of two potential plateaus, one at about 2.3 V *vs.* Li/Li^+, and the second one at about 2.1 V *vs.* Li/Li^+,[21,34,35] which represent the conver-

[a]State Key Laboratory of Advanced Technology for Materials Synthesis and Processing, International School of Materials Science and Engineering, Wuhan University of Technology, Wuhan 430070, Hubei, P. R. China. E-mail: xuxu@whut.edu.cn, mlq518@whut.edu.cn
[b]Department of Chemistry, University of California, Berkeley, CA 94702, USA

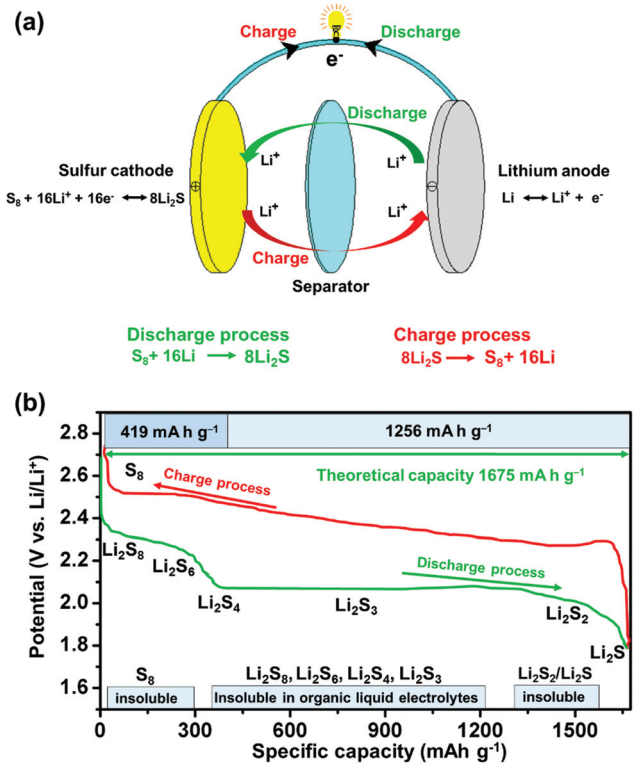

Fig. 1 (a) Schematic of the electrochemical reaction mechanism involved in a Li–S battery consisting of a sulfur cathode, separator and lithium metal anode; (b) typical discharge/charge process for a Li–S battery in an organic liquid electrolyte at room temperature.

sions of S_8 to Li_2S_4 (25% of the theoretical capacity of sulfur: 419 mA h g^{-1}) and Li_2S_4 to Li_2S (75% of the theoretical capacity of sulfur: 1256 mA h g^{-1}), respectively, as shown in Fig. 1b.[36,37] During the discharge process, S_8 reacts with lithium ions to form a series of intermediate lithium polysulfide species (Li_2S_8, Li_2S_6, Li_2S_4 and Li_2S_3), which are soluble in ether-based electrolytes. Furthermore, the reaction of lithium polysulfides with Li^+ continues to form Li_2S_2 and finally the insoluble Li_2S.[12] During the charge reaction, Li_2S is converted to S_8, also along with the generation of different intermediate lithium polysulfides.[36] Overall, the reversible conversion of S_8 undergoes a series of structural and compositional changes of complicated redox reactions, from solid to liquid then back to solid. The term "dissolution-re-deposition" is used to illustrate the electrochemical process of a Li–S battery, which is considerably different from other batteries.

1.2. The focus of this review

The chemical routes of the transition between sulfur and lithium disulfide are clearly illustrated above. However, the detailed steps involved in these route are much more complicated, and it is still not clear how the chemical and physical states of the electrode materials affect these steps during the charge/discharge process. It is commonly known that a running Li–S battery works in a closed environment, which is regarded as a black box, researchers need to open it and check the state of the electrode during the charge or discharge process, or after a given number of cycles. However, the electrochemical reaction is extremely quick, and the working electrodes are highly sensitive to the air, thus the standard *ex situ* characterization results obtained by opening the box might not be accurate.

In situ/*operando* characterization techniques can track the electrochemical reaction processes while the system is functioning, and eliminate the influence and uncertainty of the post-treatment processes of the electrode materials, which have been employed for the mechanism investigation of lithium-ion batteries to date and have achieved great success.[38,39] Naturally, these techniques have been extended to research into Li–S batteries. In recent years, various *in situ*/*operando* characterization techniques for Li–S batteries have been developed. Herein, the term "*in situ*" characterization means the measurement is carried out during the charge/discharge process of Li–S batteries. The electrochemical testing may or may not be stopped during the process, which depends on the requirement of the technique. While the term "*in operando*" characterization means the measurement is continuous during the battery testing process without interruption.[40] These *in situ*/*operando* characterization tools aim to monitor the electrochemical reaction during the charge/discharge process and obtain more detailed electrochemical information, including X-ray diffraction (XRD), transmission electron microscopy (TEM), atomic force microscopy (AFM), transmission X-ray microscopy (TXM), X-ray tomography (XRT), Raman spectroscopy, ultraviolet visible (UV-vis) absorption spectroscopy, X-ray absorption near-edge structure (XANES), nuclear magnetic resonance (NMR), high-performance liquid chromatography (HPLC), X-ray photoelectron spectroscopy (XPS), X-ray radiography (XRR), electron paramagnetic resonance (EPR)/electron spin resonance (ESR) spectroscopy, and X-Ray fluorescence (XRF). These *in situ*/*operando* characterization techniques greatly promote the in-depth understanding of the internal electrochemical processes and the degradation mechanism of the Li–S battery system. Nevertheless, there is still a lack of a comprehensive review to summarize and classify these techniques.

In this review, we summarize the development of *in situ*/*operando* characterization techniques for Li–S batteries by classifying these techniques according to the different functions and purposes (Fig. 2 and Table 1). It's worth noting that many novel *in situ*/*operando* techniques with creative designs have been employed for Li–S battery research, because the intermediate polysulfides are soluble and thus difficult to detect and track with conventional methods. Case research studies are emphasized to illustrate the degradation mechanism investigation of the system, as these can provide efficient and valuable guidance for optimization and innovation of the electrodes and electrolytes of high-performance Li–S batteries.

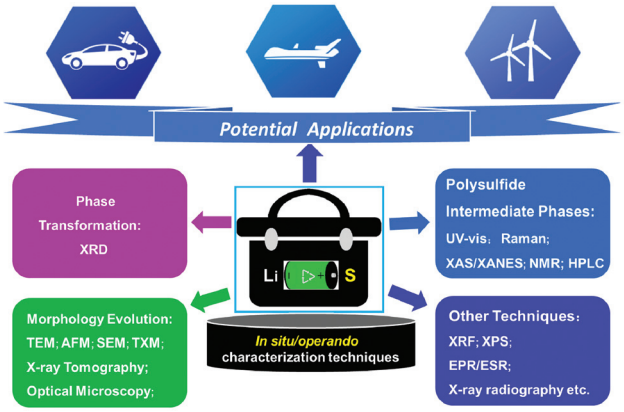

Fig. 2 Schematic showing the applications of the *in situ*/*operando* characterization tools for Li–S batteries, including the phase transformation, morphology evolution, polysulfide intermediate phases and other characterizations.

Table 1 A list of *in situ*/*operando* characterization techniques for Li–S battery research

Techniques	Unique applications
XRD	Phase transformation of crystalline sulfur and lithium sulfide during charge and discharge process
TEM	High-resolution morphological evolution of the solid phase sulfur and Li_2S
AFM	Formation of SEI
TXM	Distribution of sulfur
SEM	Morphological changes during discharge–charge cycling processes
XRT	Steric distribution of sulfur
XANES	Detection of amorphous solid phases and lithium polysulfide species
Raman	Qualitative detection of long-chain polysulfide dianions
UV-vis	Distinguishment of long- and short-chain polysulfides
NMR	Detection of the polysulfide species and the monitoring of the lithium microstructures
HPLC	Quantitative analysis of the dissolved polysulfide species and sulfur
XRR	Macroscopic structure evolution
EPR/ESR	Detection of the radical species, especially free radicals $S_3^{\bullet-}$
XPS	Interfacial chemical property evolution
XRF	The types and content of trace elements in materials

2. Phase transformation monitored by *in situ*/*operando* XRD

During the past few years, the *in situ*/*operando* XRD technique is the mostly employed characterization technique, and has been widely applied to detect the solid phase formation/consumption in Li–S batteries during the discharge and charge process.[41–53] In order to detect the discharge products, in 2012, Cui and co-workers reported *in operando* XRD characterization for Li–S batteries for the first time.[43] The authors demonstrated that the recrystallization of sulfur on the cathode after the charge process relied on the different preparation methods of the sulfur cathodes. Moreover, there was no evidence of the formation of crystalline Li_2S at the end of the discharge process (Fig. 3a–e), which was not in agreement with the most previously published *ex situ* XRD results.[54–56] The results showed that the observed crystallinity of Li_2S might be an artefact arising from the sample post-treatment. Differently, several groups demonstrated the existence of crystalline Li_2S through the lower discharge voltage plateau. In particular, Cañas and co-workers reported the formation of crystalline Li_2S at a state of discharge (60%) in the lower discharge plateau at 1.8 V. During the following charge reaction, Li_2S reacted completely and sulfur was recrystallized.[51] Similarly, Demir-Cakan *et al.*[47] and Walus *et al.*[50] also reported the formation of crystalline Li_2S on the cathode at the lower discharge plateau. These conflicting conclusions may result from different experimental set-ups and cathode compositions. Recently, crystalline Li_2S_2, a transient species, was detected by Paolella for the first time under a "solvent-in-salt" electrolyte condition.[52] In addition, Alloin and co-workers reported the co-existence of α-S_8 into β-S_8 during charge and Li_2S during discharge, and they also claimed that the Li_2S/Li_2S_2 mixture was the major discharge product.[49] The phase transformation between α-S_8 and β-S_8 was also found in other reported researches.[34,35]

However, in these *in situ*/*operando* XRD studies, the appearance of polysulfides was just presumed indirectly, whereas the direct observation of polysulfides by XRD remained challenging. In order to address this challenge, very recently, Villevieille and colleagues reported the direct detection of discharge intermediate products adsorbed on the surface of glass fibres with fumed SiO_2 using an *operando* XRD technique, which enabled them to interpret the mechanism of polysulfide formation and the evolution of a Li–S battery (Fig. 3f–h).[41] Using this approach, the polysulfides became visible under X-rays. On the other hand, they demonstrated that fumed SiO_2 was a potential electrolyte additive, which could greatly improve the performance of Li–S batteries, because SiO_2 can enable the organized adsorption of the long-chain polysulfides. Despite that the introduction of SiO_2 as a polysulfide scavenger to improve the Li–S battery performance has been demonstrated before,[57] this work is certainly creative and very significant for any future efforts in this field.

3. *In situ*/operando morphological characterization techniques

The morphology of the electrode material in rechargeable Li–S batteries is a critical factor for optimizing the performance. To date, many *in situ*/*operando* techniques have been applied in model batteries consisting of a working electrode, a counter electrode and an electrolyte assembled within the advanced equipment for the investigation of the interfacial reaction processes. Electrochemical reactions often occur at the nanoscale, so electron microscopy plays an indispensable role in monitoring the morphology and uniformity of electrode microstructures, including TEM, AFM, SEM, TXM, XRT, *etc.*

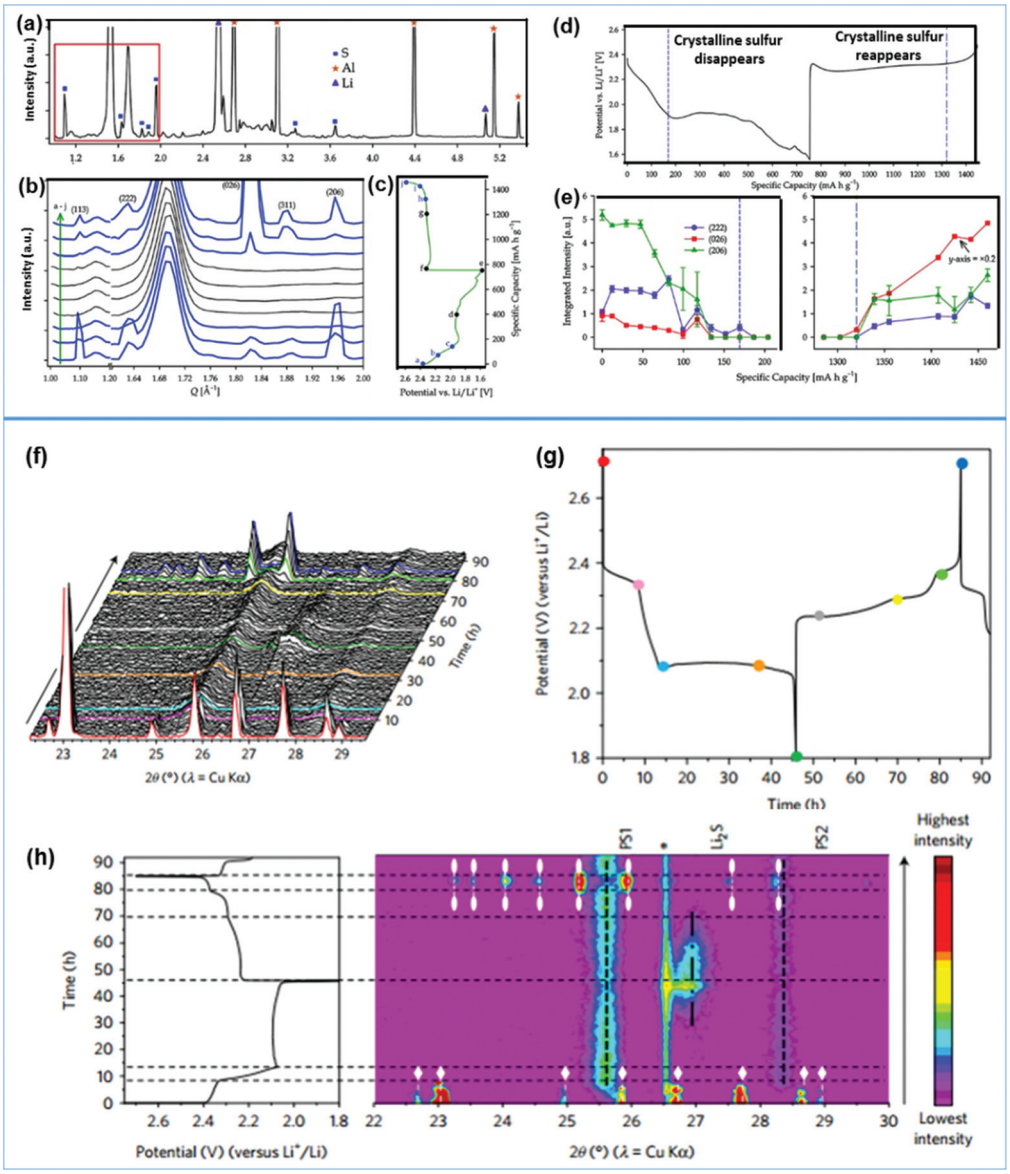

Fig. 3 Schematic and examples of *in operando* XRD measurements of Li–S batteries. (a–e) The battery was cycled with a sulfur/Super P composite electrode material at C/8. (a) XRD pattern at the start of the discharge process; (b) XRD patterns for the region of Q-space marked by the red box in (a); (c) the corresponding voltage profile; (d) integrated diffraction-peak intensities of elemental sulfur, and the corresponding voltage profile. (f–h) The battery was investigated by using fumed SiO_2 as an electrolyte additive to exploit its adsorption of polysulfides during the first cycle of the Li–S battery at a C/50 rate. (f) Waterfall representation of the XRD patterns; (g) the corresponding discharge/charge curve; (h) XRD contour plot of the data shown in f, with the same discharge/charge curve as shown in g. ((a–e) Adapted with permission from ref. 43, Copyright (2012) American Chemical Society. (f–h) Reprinted with permission from ref. 41, Copyright (2017) Macmillan Publishers Ltd.)

3.1. TEM

The *in situ* TEM technique provides real-time comprehensive information of the electrode during electrochemical reactions at a high spatial resolution, such as the microstructure evolution and the chemical composition changes.[58–60] *In situ* TEM has been employed in Li–S battery research to monitor the morphological changes of the solid phase sulfur and Li_2S.[61–63] For instance, inspired by the unique flexibility and strong interlayer van der Waals interaction of two-dimensional (2D) materials,[58,64] Tang *et al.* used solution-exfoliated MoS_2 flakes to capture sulfur particles, and studied the detailed discharge/charge processes by utilizing *in situ* TEM,[61] where the *in situ* TEM set-up was similar to those in the previously reported works (Fig. 4a).[63,65–68] The morphology variation of the MoS_2-encapsulated sulfur spheres was highly reversible during the discharge and charge processes, with an illustration of this shown in Fig. 4b. Meanwhile, they revealed that the active sulfur particles can be hermetically confined within this 2D material. In 2016, Kim *et al.* reported on their dynamic investi-

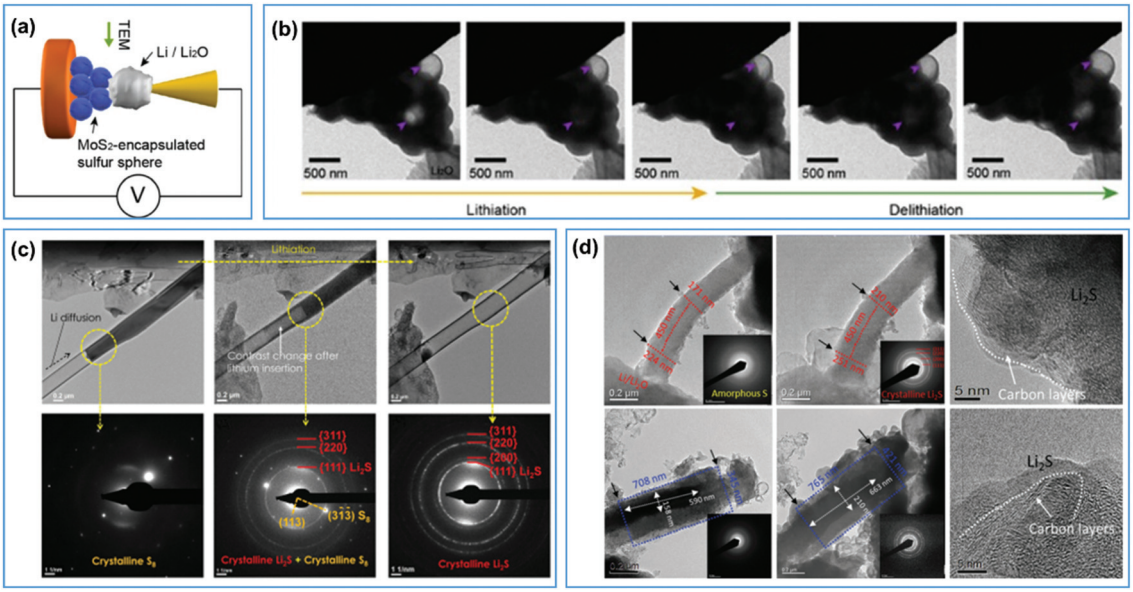

Fig. 4 (a) Schematic of the *in situ* TEM experiment set-up with MoS_2-encapsulated hollow sulfur spheres; (b) selected real-time images of the electrode material evolution during the typical lithiation–delithiation process of MoS_2-encapsulated hollow sulfur spheres to demonstrate the high reversibility. (c) *In situ* TEM images adopted with S confined in a carbon nanotube during lithiation reaction and their corresponding EDP patterns. (d) Collected *in situ* TEM images and corresponding SAED patterns with PCNF/A550/S, where the letters a, d present the initial state, letters b, e present full lithiation, letters c, f present high resolution TEM images of lithiated PCNF/A550/S (c) PCNF/A750/S (f). ((a, b) Reproduced with permission from ref. 61, Copyright (2017) American Chemical Society; (c) reproduced with permission from ref. 62, Copyright (2015) Wiley-VCH; (d) reproduced with permission from ref. 63, Copyright (2017) Wiley-VCH.)

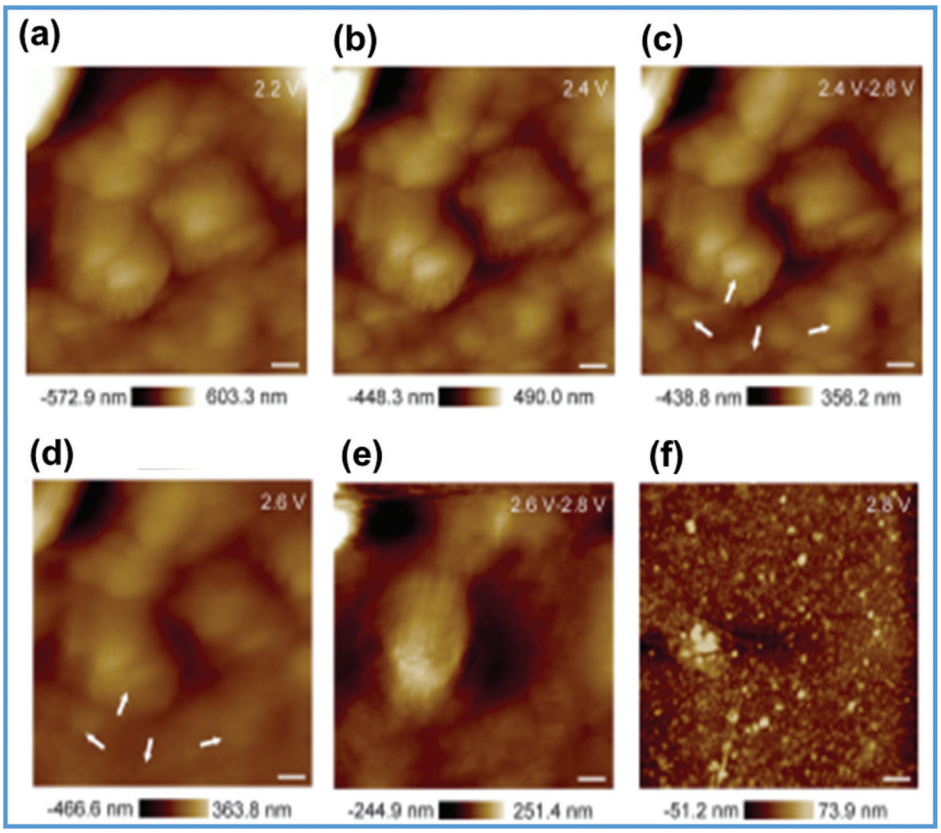

Fig. 5 *In situ* AFM surface topography images at different potentials. (Adapted with permission from ref. 70, Copyright (2016) Wiley-VCH.)

gations of the lithiation of sulfur active particles confined within a carbon nanotube.[62] With their *in situ* TEM study, the authors demonstrated that it was possible that the S to be directly transformed into Li_2S (Fig. 4c) without the formation of lithium polysulfide phases with a high solubility in the commonly used electrolytes, and their study may help to address the ongoing issues in Li–S battery technology. Afterwards, Xu *et al.* also reported the volume expansion of porous carbon nanofibre/S composite cathode materials under high-rate conditions using *in situ* TEM examination (Fig. 4d), which provided new and valuable insights into the correlation between the electrochemical performance and the volume expansion.[63]

3.2. AFM

The *in situ* TEM technique mainly highlights the direct observation of the morphology evolution, whereas *in situ* AFM analysis can readily incorporate environmental conditions that mimic the cell environment at the nanoscale, and can be used to track the evolution of the surface topography under such conditions. Furthermore, *in situ* AFM can provide access to probing the formation of the solid electrolyte interface (SEI) layers during battery cycling.[69] In 2016, Wan and co-workers creatively employed the *in situ* AFM technique to probe the dynamic nucleation, growth, dissolution and re-deposition processes of insoluble Li_2S_2 and Li_2S at the positive electrode/electrolyte interface in Li–S batteries (Fig. 5).[70] Furthermore, the authors combined other characterization techniques, including X-ray photoelectron spectroscopy (XPS) and Raman spectroscopy, to provide deep insights into the structure–reactivity correlation and performance fading mechanism of Li–S batteries at the nanoscale. Their findings offered a direct visualization of the interfacial structure and a constructive guideline to design better electrode materials for Li–S batteries.

3.3. TXM

The application of TXM in energy storage systems can provide non-destructive, high-resolution (tens of nanometres) X-ray images of the active electrode materials during electrochemical cycling, and provide some extra chemical information.[71,72] Recently, the *in situ* TXM analytical technique was established by Cui and co-workers for the application in Li–S batteries for the first time, to track the dissolution and solidification of the composite sulfur electrode during constant current discharge–charge processes, where the sample holder plates of *in operando* TXM are exhibited in Fig. 6a. Surprisingly, from the TXM analysis of the dimensional variations of an individual sulfur active particle in a working battery, the authors observed very little change in the sulfur particle size, which was considerably different from what would be expected from lithium polysulfide species dissolution, resulting in the crystallization of S_8 or elemental S at the end of charging.[43] The micrographs of a sulfur composite particle at various potentials during the discharge process are shown in Fig. 6c, in which the letters correspond to the points marked as a–i in Fig. 6b. In addition, in 2014, Lin *et al.* reported that S particles exhibited complicated dimensional changes in working batteries based on *in operando* TXM.[73] The authors observed an intense shrinkage and expansion of S particles caused by polysulfides dissolution and re-deposition, respectively. Furthermore, they claimed that the dissolution rate of lithium polysulfides depended on the

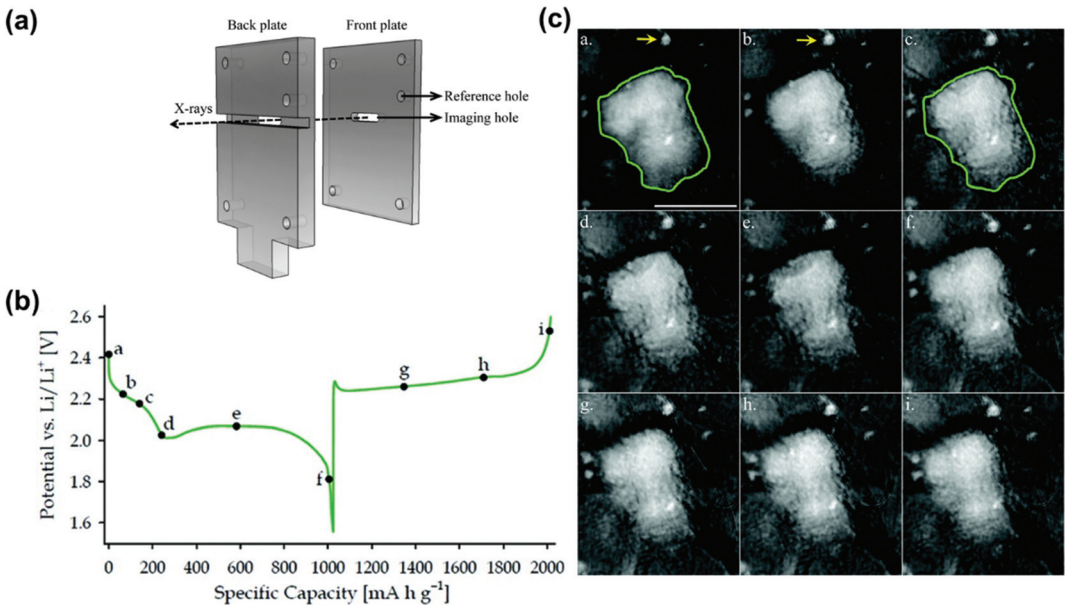

Fig. 6 (a) Sample holder plates of *in operando* TXM; (b) discharge and charge process voltage profiles *versus* specific capacity of a Li–S battery cycled at C/8, where the letters a–i correspond to the capacities at different voltages; (c) *in operando* TXM images of a sulfur composite particle during electrochemical cycling, where the letters correspond to the points labelled a–i in (b). (Adapted with permission from ref. 43, Copyright (2012) American Chemical Society.)

lithium stoichiometry and that polysulfides re-deposition was nucleation-limited, and also reported an extensive aggregation of lithium polysulfides, leading to tremendous dimensional variations of active sulfur particles and undesirable cycling stability.

3.4. Other morphological characterization techniques

In situ/*operando* SEM can monitor the morphological changes during discharge–charge cycling to provide insights into the preferred reaction sites of the electrode.[74,75] Marceau *et al.* combined *in situ* SEM and *in operando* UV-vis techniques to gain a clear understanding of the degradation mechanisms of Li–S batteries.[74] Zhang and Cui discovered a new-generation of highly nitridated graphene/Li_2S as the positive electrode materials of Li–S cells, which could be highly stable for hundreds or even thousands of cycles. By a newly designed *in situ* SEM set-up, the authors observed that the Li_2S particles on graphene became smaller and smaller during charging, which was mainly caused by the dissolution of lithium polysulfides into the electrolyte. Moreover, they found that the design of the new electrode materials and the new recharge protocol could offer a promising method for the practical application of high energy density Li–S batteries.[75]

Owing to the non-invasive and non-destructive nature, XRT has been extensively used to investigate the micromorphology of electrode materials in LIBs;[76–81] however, the usage of this technique was not introduced in Li–S battery research until 2016. Yermukhambetova *et al.* employed a multi-scale three-dimensional (3D) *in situ* tomography approach to characterize the morphological parameters and track the microstructural evolution of the sulfur phase through discharge/charge cycles.[82] They expected that X-ray tomography would be a powerful characterization technique for the designation and optimization of electrode materials for Li–S batteries.

In 2014, Cui's group designed a Li–S battery to directly visualize the spatial and temporal distribution of lithium polysulfide species though the entire electrochemical cycles under optical microscopy.[83] This technique was a quick method to determine the limitation effect of polysulfide diffusion in sulfur electrodes and through Nafion-modified separators.

4. *In situ*/*operando* detection and tracking of soluble polysulfides

In a Li–S battery system, *in situ*/*operando* characterization techniques for phase transformation and morphology evolution are only valid for the solid phases, including sulfur, Li_2S and Li_2S_2, because the intermediate long-chain lithium polysulfides are soluble in the commonly used ether-based electrolyte. However, the detailed chemical transition of lithium polysulfides with different chain lengths and the interaction between them and the electrodes are extremely important for a full understanding of the entire electrochemical reaction route in Li–S chemistry. In this section, some novel *in situ*/*operando* characterization techniques specifically designed for the detection and distinguishment of polysulfide species are summarized, mainly those involving X-ray absorption structure (XAS), UV-vis, Raman, NMR, and HPLC.

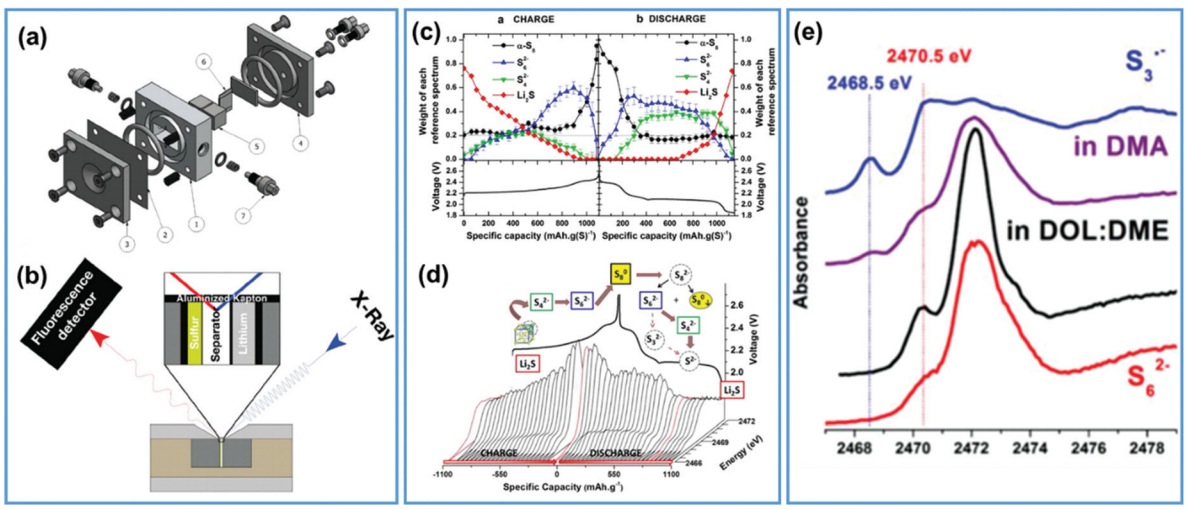

Fig. 7 *In situ* XANES tests of Li–S batteries. (a) Schematic of the spectra-electrochemical *in operando* battery, corresponding to its individual components; (b) schematic of the *in operando* XANES set-up that allows detection of X-ray fluorescence from all layers in the cell. (c) A linear combination analysis of sulfur K-edge XANES based on charge/discharge cycling, four compounds (α-S_8, S_6^{2-}, S_4^{2-} and Li_2S) were utilized as reference materials; (d) *in situ* XANES during the electrochemical cycle and the proposed reaction mechanism for Li–S cells. (e) Experimental *in operando* XANES around 340 mA h g^{-1} collected during discharge in Li–S batteries using DMA or DOL : DME electrolytes compared, with $S_3^{\bullet-}$ and S_6^{2-} as reference materials. ((a, b) Reproduced with permission from ref. 84, Copyright (2015) Manchester Nh: Electrical Society; (c, d) reprinted with permission from ref. 86, Copyright (2013) American Chemical Society; (e) reproduced with permission from ref. 94, Copyright (2015) Wiley-VCH.)

4.1. XAS

Synchrotron XAS can unveil the element-specific information, which does not require the sample to be crystalline or in an amorphous phase. It can help researchers to improve their knowledge to decide the chemical component of each electrode material under charge/discharge conditions, with the sulfur K-edge spectrum mainly applied to identify different sulfur-containing species.[45,84–92] Generally speaking, the spectrum of XAS can be divided into three parts: the pre-edge, XANES and the extended X-ray absorption fine structure (EXAFS). Among these, XANES is often employed to investigate the composition, providing important insights into the working mechanism of Li–S batteries.[45,84,91–94] When using the *in situ* XANES technique, the battery should be delicately designed. For example, an *in operando* XANES set-up was designed by Gorlin *et al.* with the X-ray window on the side of the battery (Fig. 7a and b), which ensured that the information could be adopted at the whole depth of the positive electrode and separator.[84] By applying *in operando* XANES spectroscopy on the S K-edge, Nazar's group detected various polysulfides in a working Li–S battery during the discharging–charging process. To accurately monitor S or lithium polysulfide species, they prepared and calibrated reference standards of S_8, S_6^{2-}, S_4^{2-}, S_3^{2-} and S^{2-} (Fig. 7c), and the XANES results revealed detailed evidence of the electrochemical mechanisms of sulfur redox chemistry during the cycling process. In addition, compared with batteries utilizing the conventional ether-based electrolyte, when using dimethyl acetamide (DMA) as the electrolyte, a three-plateau reduction reaction[86,95] could be observed by *in operando* XANES (Fig. 7d).[86] In particular, the appearance of $S_3^{\bullet-}$ in DMA was confirmed (Fig. 7d and e).[86,94] Generally, the concentration of $S_3^{\bullet-}$ ($\ll$5%) was measured by XANES, which was utilized to prove the cleavage of dianions S_6^{2-}.[84,86,94,96] There is a characteristic pre-peak at around 2468.5 eV in the XANES analysis (Fig. 7e),[94] which was applied to illustrate the existence of the radical anion ($S_3^{\bullet-}$) in Li–S batteries. Although researchers have accessed the absorption spectra of different polysulfides, there are only two kinds of polysulfide dianions to quantify the analysis from working

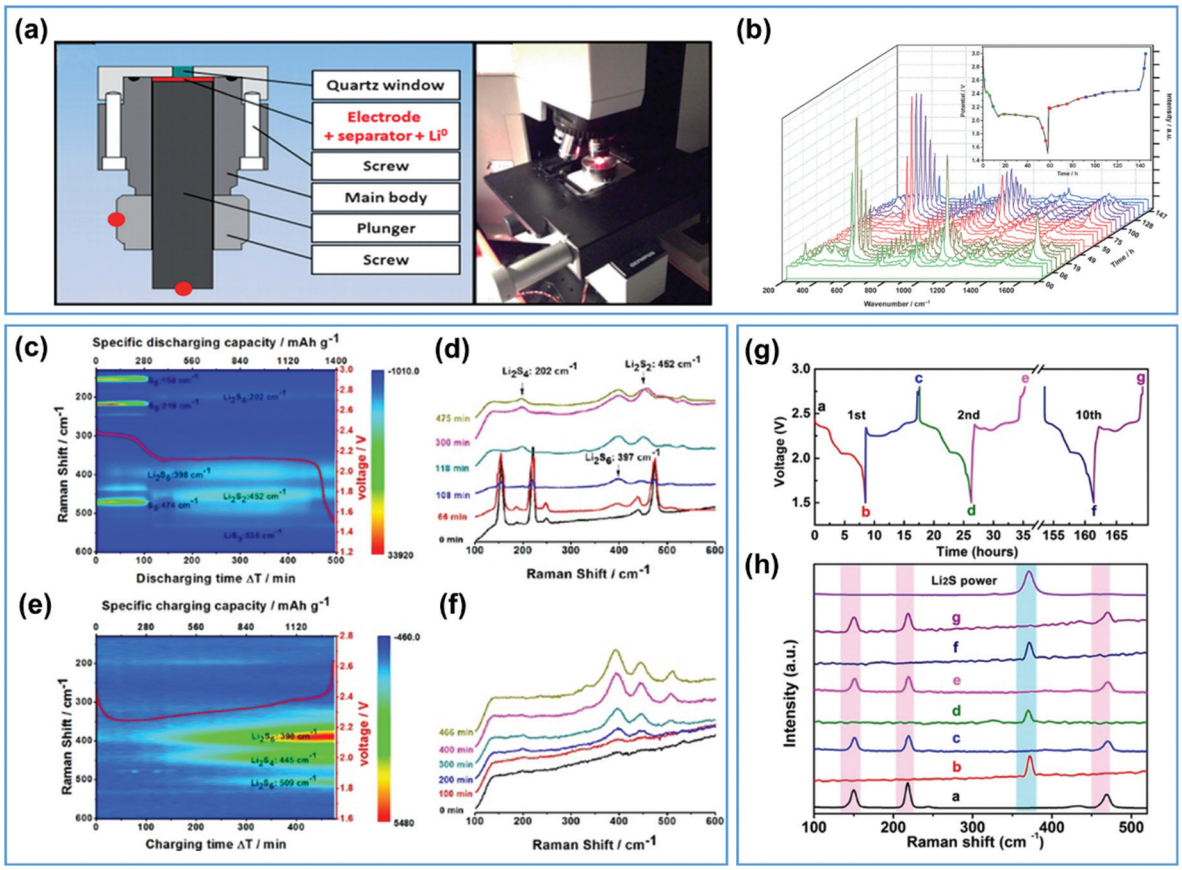

Fig. 8 *In situ* Raman measurements of a Li–S battery. (a) Schematic of the *in situ* Raman experiment set-up of positive carbon–sulfur (C/S) composite electrodes; (b) real-time Raman spectra, corresponding the Li–S battery electrochemical response at C/60 during the first discharging-charging cycle. (c–f) The battery was cycled with N-doping super P carbon/sulfur. (c and e) *In situ* Raman spectra obtained during discharge and charge reactions, respectively; (d and f) the obtained *in situ* Raman spectra, corresponding to (c) and (e). (g, h) The battery was cycled with the positive electrode of nanosulfur particles on Ni foam at C/10. (g) The discharge and charge processes; (h) collected *in situ* Raman spectra from the points labelled a–g in (g) of a Li_2S powder. ((a, b) Reproduced with permission from ref. 109, Copyright (2015) Wiley-VCH; (c–f) reproduced with permission from ref. 108, copyright (2015) American Chemical Society; (g, h) reproduced with permission from ref. 102, Copyright (2015) American Chemical Society.)

batteries.[86,91,94,97] It is worth noting that a great deal of efforts of *in operando* XANES research should be devoted to exploit and calibrate a comprehensive absorption spectra, which is of great significance for further investigation.

4.2. Raman spectroscopy

For Li–S battery research, Raman spectroscopy can probe the polarizable surface with low concentrations in vibrational energy levels, and enable the detection of the transient states of an electrode surface. In addition, it can qualitatively or semi-quantitatively detect the lithium polysulfides dissolved in a conventional ether-based electrolyte during the discharge–charge processes of Li–S batteries, which is considerably significant for researchers to estimate the condition of an electrode material in the liquid phase. Typically, Raman shifts (fundamental frequency) of polysulfide dianions and radicals are all below 550 cm^{-1}.[98–103] It is important to learn that the characteristic peaks of S_8 are located around 150, 219 and 474 cm^{-1}.[100] The high-order polysulfide dianions (S_8^{2-}, S_6^{2-} and S_4^{2-}) can be captured by Raman spectra, while the low-order ones cannot ($S_3^{2-}$and S_2^{2-}).[104–107] Additionally, the peak signal of the radical anion ($S_3^{\bullet-}$) at 525–535 cm^{-1} could be detected, which is in good agreement with most theoretical and experimental studies.[107,108] For instance, Hannauer *et al.* designed an *in operando* Raman set-up (Fig. 8a) to monitor the evolution of various possible polysulfides. The Li–S battery was cycled with a cathode of active carbon/sulfur composites to obtain Raman spectra during the first galvanostatic cycle (Fig. 8b).[109] Dong and co-workers developed a conductive Lewis-base matrix as the positive electrode material for Li–S batteries. By combining *in operando* Raman spectroscopy and density functional theory (DFT) methods, they extracted and were able to understand the complicated chemistry of Li–S batteries. Experimentally, Li_2S_8 was found to be missing during the whole redox route and the charging process ended at Li_2S_6, as shown in the corresponding illustration in Fig. 8c–f.[108] Chen's group also elucidated the sulfur redox mechanism of Li–S batteries with S nanodots electrodeposited on a Ni-foam as the cathode, which showed high electrochemical performance. By using *in situ* Raman spectra, several charge/discharge cycles (Fig. 8g and h) exhibited the reversible reaction between S and Li_2S.[102]

4.3. UV-vis spectroscopy

Different from Raman spectroscopy, UV-vis spectroscopy is a kind of absorption spectroscopy with a series of absorption bands in the UV-vis spectral region, which has been well proven as a powerful characterization method to analyse solution-based electrochemical reactions, and therefore has been widely employed for the qualitative and quantitative detection of lithium polysulfide species in Li–S batteries.[110–119] Generally, S_8 or elemental S shows a characteristic absorption peak around 270–280 nm.[113,120] Polysulfide dianions correspond to the absorption bands in the range of 350 to 500 nm, and the radical $S_3^{\bullet-}$ has a relative strong absorption around

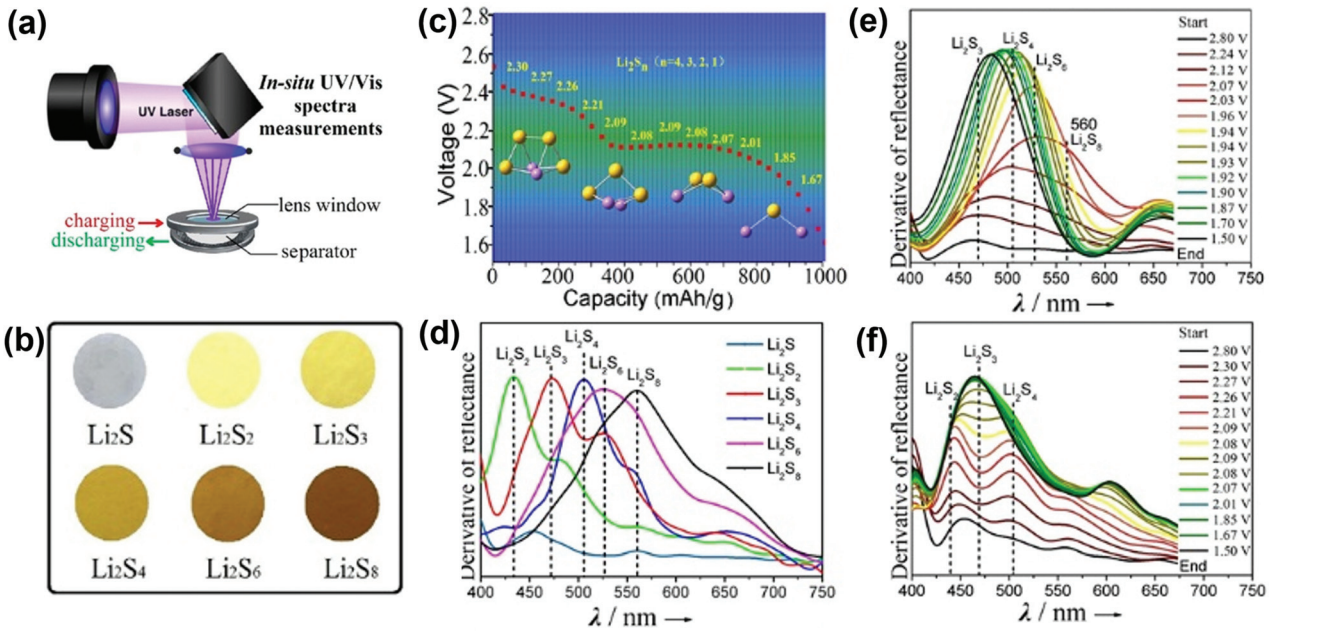

Fig. 9 (a–f) *In operando* UV-vis spectra detected during the first discharge of a Li–S battery (a) the battery unit with a sealed glass window for *in operando* UV-vis set-up. (b) Photographs of six different catholyte solutions; (c) the collected discharge voltages were used for the *in situ* UV-vis mode; (d) the corresponding UV-vis spectra first-order derivative curves of different stoichiometric compounds; the corresponding UV/vis spectra first-order derivative curves of (e) rGO/S and (f) GSH/S electrodes at C/3, respectively. ((a–f) Adapted with permission from ref. 121, Copyright (2017) American Chemical Society.)

620 nm.[113,115,117,121] In order to obtain the information of *in operando* UV-vis absorption spectra from a working Li–S cell, the reflection configuration was designed by Dominko and co-workers for the first time.[111,122] By demarcating the spectra of chemically synthesized lithium polysulfide solutions, qualitative and quantitative analyses were realized. Afterward, Marceau *et al.* further combined *in operando* SEM and *in operando* UV-vis to detect and identify the formation of sulfur species.[123] As a result, a clearer understanding of the degradation mechanisms of Li–S batteries was required. Their findings implied that the discharge and charge processes are not completely reversible and proceed along different pathways. Very recently in 2017, Yan and co-workers used a reflection-mode (Fig. 9a) to detect the lithium polysulfides of a Li–S battery in the electrolyte during discharge/charge cycling.[121] In order to distinguish the long- and short-chain polysulfides, the authors prepared six different samples (Li_2S_2, Li_2S_2, Li_2S_3 Li_2S_4 Li_2S_6 and Li_2S_8). When these polysulfides were dissolved in the electrolyte, the colour of the electrolyte changed from transparent to dark red (Fig. 9b). It is noteworthy that the selected discharge voltages were applied during *in situ* UV-vis measurements (Fig. 9c), and the absorption wavelength of the measure reflectance was used as a function of the state of the battery in the UV-vis spectrometry analysis. They discovered that the peaks at 530 and 560 nm corresponded to the long-chain Li_2S_6 and Li_2S_8 during the initial discharging process, respectively. Along with further discharging, the peaks at 435, 470 and 505 nm were ascribed to the formation of short-chain Li_2S_2, Li_2S_3, and Li_2S_4, respectively. During the discharge process, the short-chain Li_2S_2 and Li_2S_3 polysulfides were detected as the main intermediates, corresponding to the elucidation in Fig. 9d–f. Differently, Lu and co-workers revealed solvent-dependent Li–S redox pathways with *in operando* UV-vis spectroscopy. It should be pointed out that the sulfur redox reactions have an obvious difference in two different solvents.[117] By using this strategy, it may open up valuable insights into the fundamental research for the practical application of Li–S batteries. Also, Yan and co-workers reported a new strategy that the volumetric capacity and Coulombic efficiency can be improved by selenium doping for lithium-organosulfur batteries. By means of the *in situ* UV-vis technique, they found that the shuttle effect was efficiently weakened since no long-chain polysulfides were generated during the entire cycling process resulting from selenium doping (Fig. 9g–i).[119] Although *in situ* UV-vis spectroscopy has been developed to help researchers understand the mechanism of Li–S batteries, more effort is required to establish a set of standardized absorption peaks for a more accurate and detailed acquisition of data.

4.4. NMR spectroscopy

Owning to the high sensitivity of ^{7}Li NMR to ^{7}Li nuclei, the ^{7}Li signal (spin = 3/2, 92.5% abundance) can be nicely captured on a timescale that is much faster than the discharge–charge cycle.[124,125] Herein, *in situ* and *ex situ* ^{7}Li NMR have been mainly applied in Li–S systems to detect different soluble polysulfides.[126–128] Performing *in situ* NMR in Li–S batteries during electrochemical cycling can assist dynamically monitoring the growth and stripping of lithium microstructures. With an in-house cylindrical microbattery designed for *in situ* NMR (Fig. 10a), the phase evolution of the lithium metal anode entangled with parasitic reactions was recorded (Fig. 10b and c).[129] With *in situ* NMR spectroscopy, Seshadri and co-workers directly observed the soluble Li^+-species during battery discharge, which was known to be highly detrimental to the capacity retention (Fig. 10d and e). They also confirmed that the formation of a solid component (Li_2S) started at the beginning during the first discharge plateau.[130] Subsequently, in 2017, Wang *et al.* proposed a comprehensive approach to quantitatively detect the changes of all lithium polysulfide species in Li–S batteries during discharge–charge cycling by *in situ* NMR spectroscopy.[131] Metallic lithium evolution upon discharge/charge cycling and mossy lithium formation with time were exhibited, respectively. Their detections provided tremendous assistance for the electrolyte development, sulfur cathode study and for lithium metal protection strategies.

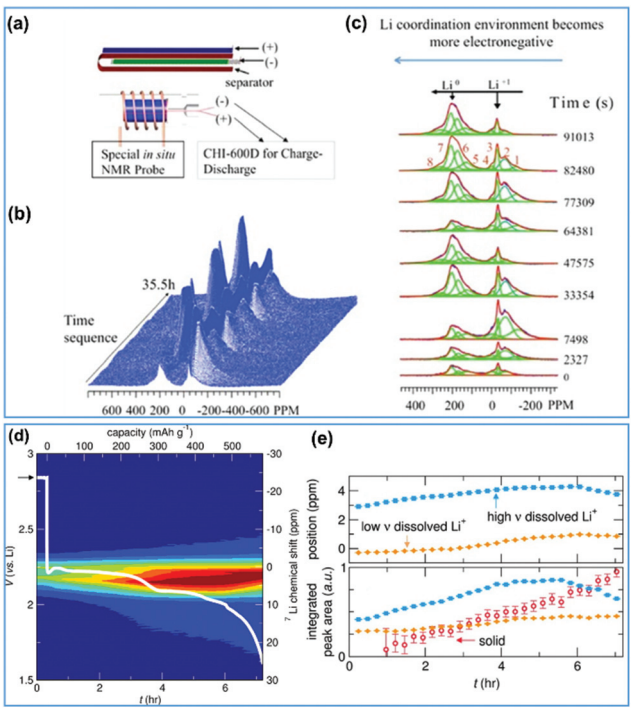

Fig. 10 (a) Schematic of *in situ* NMR experiments set-up with an in-house cylindrical microbattery; (b) obtained time sequence ^{7}Li NMR spectra in an operating Li–S microbattery during discharge/charge; (c) main peaks were extracted at different times by fitting the spectra. (d, e) A Li–S battery was cycled at C/20. (d) *In situ* ^{7}Li NMR signal overlaid on the electrochemical discharge curve; (e) the changes in chemical shift and integrated intensities as a function of discharge. ((a–c) Reprinted with permission from ref. 129, Copyright (2015) American Chemical Society; (d–f) reprinted with permission from ref. 130, Copyright (2014) American Chemical Society.)

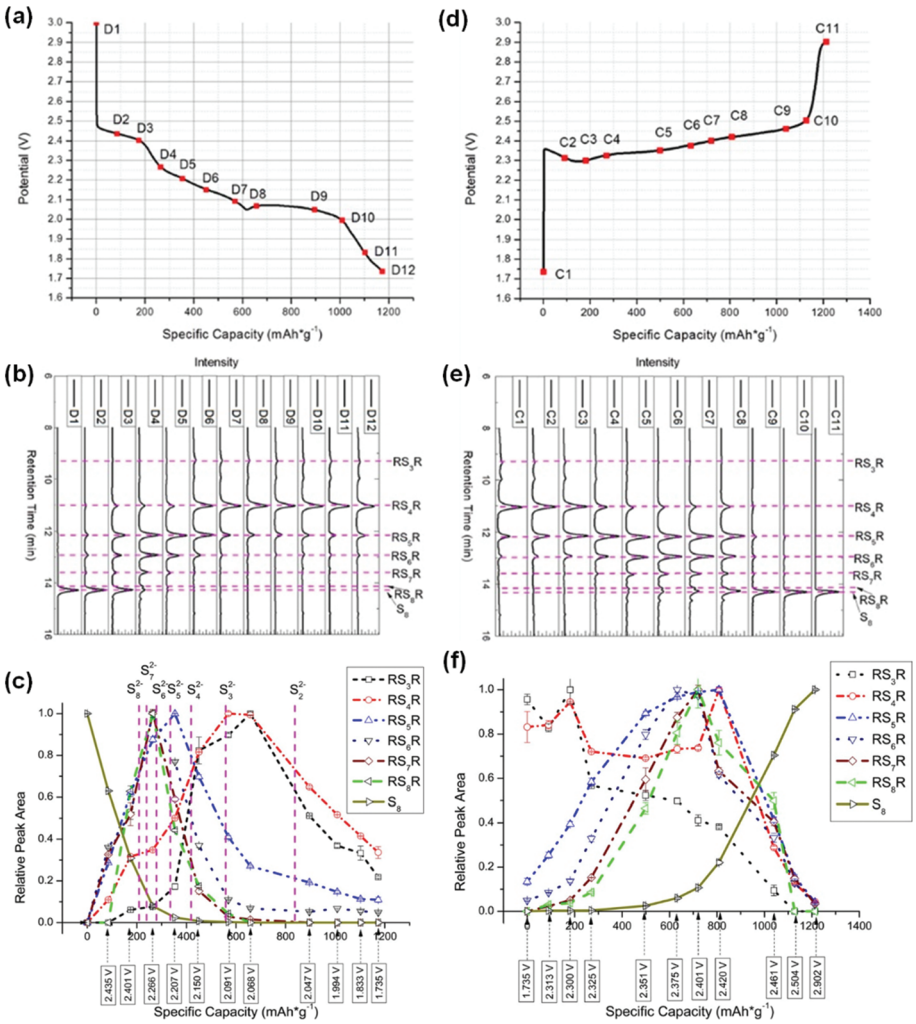

Fig. 11 The battery was cycled at C/70. (a) Discharge profile of the Li–S battery with sampling points (red squares from D1 to D12) during operation, (b) the corresponding HPLC chromatograms with (a), (c) standard chromatographic peak for each parasitic polysulfide species (R = CH_3) from real-time HPLC results during discharging, (d) charge profile of the Li–S battery with sampling points (red squares from C1 to C11) during operation, (e) the corresponding HPLC chromatograms with (d) and (f) standard chromatographic peak for each parasitic polysulfide species (R = CH_3) from real-time HPLC results during charging. (Adapted with permission from ref. 95, Copyright (2016) American Chemical Society.)

4.5. HPLC

HPLC is a powerful separation technique that is widely applied in qualification as well as quantitation. Recently, by utilizing this technique, researchers could determine the dissolved polysulfide ions in the electrolyte of Li–S batteries.[95,120,132–135] For instance, Zheng *et al.* reported a systematic study of the real-time quantitative determination of lithium polysulfide intermediates and sulfur by means of an HPLC technique during discharge and charge processes.[95] The change from elemental sulfur to long-chain polysulfide intermediates, and then to short-chain polysulfide intermediates could be clearly confirmed as the discharge reaction (Fig. 11a–c). From the charge process (Fig. 11d–f), the valuable conclusion is that almost all of the solid lithium sulfides (Li_2S and Li_2S_2) and dissolved lithium polysulfide species became oxidized back to elemental sulfur (S_8). Most importantly, their findings provided a valuable supplement to the information from other characterization techniques, and further assisted gaining a comprehensive and clear understanding of the redox mechanism of the Li–S battery.

5. Other *in situ*/*operando* characterization techniques

In this section, several other *in situ*/*operando* characterization techniques are summarized, which provide some new insights and strategies in Li–S battery research.

5.1. XRR

Risse *et al.* presented a multi-dimensional set-up, which combined electrochemical impedance spectroscopy (EIS), constant current charging and discharging and X-ray radiography to study Li–S batteries (Fig. 12a).[136] Based on this set-up, the

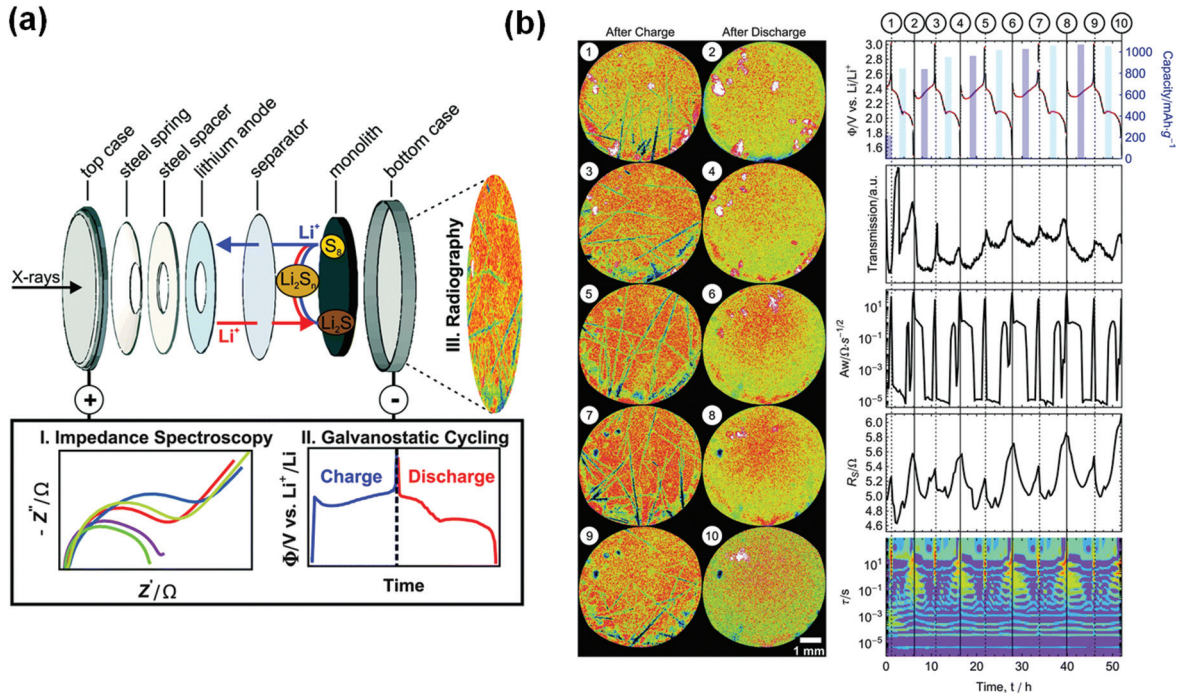

Fig. 12 (a) Schematic set-up of the *operando* battery combining *operando* X-ray radiography with electrochemical impedance spectroscopy and galvanostatic charge/discharge cycling. (b) A multi-dimensional *operando* analysis of the first five cycles at C/10. The numbers in the voltage-time curve with the respective electrochemical capacities (blue bars), overall transmittance, Warburg coefficient, solution resistance and the distribution of relaxation times, corresponding to the radiography images points labelled 1–10 on the left. (Reproduced with permission from ref. 136, Copyright (2016) Royal Society of Chemistry.)

authors acquired radiography images and a voltage–time curve with the respective electrochemical capacities (blue bars), overall transmittance, Warburg coefficient, solution resistance and the distribution of relaxation times (Fig. 12b). The entire research clearly exhibited the power of a multi-dimensional *in operando* study of the Li–S battery system. Yang *et al.* also reported their research results by applying *in operando* measurements,[137] using a similar set-up to that developed by Risse *et al.*[136]

5.2. XPS

In order to gain an integrated understanding and molecular-level insight of the sulfur redox reactions and subsequent evolution mechanism of the SEI layer at the Li-metal anode in Li–S batteries, Murugesan and co-workers reported the first application of *in situ* XPS for a Li–S battery, to provide not only the spatially resolved chemical imaging, but also lithium polysulfides speciation *via* high-resolution core-level spectroscopy of the critical elements.[138] The key issues and major challenges are the high vapour pressures of elemental sulfur (S_8) and the aprotic electrolyte solvents (1,3-dioxolane (DOL) and dimethoxyethane (DME)) in characterizing *in situ* XPS for Li–S batteries. In order to overcome these issues, the authors utilized an ultrahigh vacuum (UHV) compatible 1-butyl-1-methylpyrrolidinium bis(trifloromethylsulfonyl)imide ($[bmpyr]^+[TFSI]^-$) ionic liquid (IL) as a cosolvent in the electrolyte. Moreover, this kind of ionic liquid with high electrochemical stability has been reported as an electrolyte solution for Li–S batteries that are electrochemically stable in the voltage range (±2.2 V).[139,140] Ultimately, the authors claimed that it was crucial for controlling the role of the SEI layer in Li–S batteries during cycling processes.

5.3. EPR/ESR

With spin traps, the unpaired electrons of the reaction intermediates can be stabilized and detected by the EPR/ESR technique. Furthermore, the application of the *in situ* EPR/ESR technique has been reported to directly observe the formation and evolution of $S_3^{\bullet-}$ radicals during the electrochemical process in Li–S batteries.[141] The authors revealed that the generation and concentration of sulfur radicals was found to change periodically at various potentials, providing valuable information for the interplay between the chemical and electrochemical reactions in Li–S batteries.

5.4. XRF

XRF microscopy is used as a novel and powerful characterization technique to decide the types and content of trace elements in materials. In 2015, Yang and co-workers reported an *in situ* XRF study for Li–S batteries.[142] By collecting images of the electrode in real time during the first cycle, redistribution of the S_8 or elemental S and lithium polysulfides reduction of Li–S electrochemical system was directly observed.

6. Summary and outlook

A fundamental understanding of the electrochemical route and the interactions between the components in a Li–S battery can provide guidance for the further development of practical Li–S batteries with high energy density and a long cycle life. *Ex situ* techniques have been mainly used because of their easy access and low lost. However, the results might not be accurate enough due to the necessary post-treatment and the time delay. *In situ*/*operando* techniques for Li–S battery research have achieved exciting progress in recent years, which is systematically summarized and classified in this review by the functions.

In situ/*operando* techniques have greatly promoted a greater understanding of the reaction mechanism of Li–S batteries; however, their widespread utilization is still limited. First, *in situ*/*operando* characterization techniques often require high-cost facilities and complex experimental set-ups, resulting in an unacceptable high cost and inconvenience for the researchers. On the one hand, conventional chemical or physical analytical techniques should be creatively introduced and specially designed for the *in situ*/*operando* characterization of Li–S batteries, such as *in situ*/*operando* UV-vis spectroscopy, which shows great potential in this field. On the other hand, opening up the large advanced facilities, such as the synchrotron light sources, to academic institutions would also be helpful in this regard. Second, the spectroscopic methods have been proven to be a powerful tool for the detection of the intermediate polysulfides. A complete and accurate fingerprint database for polysulfide species would be helpful for distinguishing different species, which is critical for a further understanding of the electrochemical reaction route of the Li–S battery.

In addition, each method can capture only part of the information in the working system, and different characterization methods with different cell configurations may lead to an inconsistent understanding of the detailed electrochemical reaction steps, thus the combination of different *in situ*/*operando* techniques would provide more comprehensive information for researchers.

Although there are many challenges, we optimistically anticipate that, with the better understanding of the mechanism, Li–S batteries will realize practical application in the near future. We believe that *in situ*/*operando* characterization techniques will keep playing an important role towards this goal.

Conflicts of interest

The authors declare no conflict of interest.

Acknowledgements

This work was supported by the National Key Research and Development Program of China (2016YFA0202603, 2016YFA0202604), the National Basic Research Program of China (2013CB934103), the National Natural Science Foundation of China (51702247, 51521001, 51502227 and 51579198) and the National Natural Science Fund for Distinguished Young Scholars (51425204), the Fundamental Research Funds for the Central Universities (WUT: 2017-III-005, 2017-III-030). Prof. L. Q. M. gratefully acknowledges financial support from the China Scholarship Council (No. 201606955096).

Notes and references

1 J. W. Choi and D. Aurbach, *Nat. Mater.*, 2016, **1**, 16013.
2 H. D. Lim, B. Lee, Y. Zheng, J. Hong, J. Kim, H. Gwon, Y. Ko, M. Lee, K. Cho and K. Kang, *Nat. Energy*, 2016, **1**, 16066.
3 M. C. Lin, M. Gong, B. Lu, Y. Wu, D. Y. Wang, M. Guan, M. Angell, C. Chen, J. Yang and B. J. Hwang, *Nature*, 2015, **520**, 325–328.
4 J. B. Goodenough, *Energy Environ. Sci.*, 2013, **7**, 14–18.
5 M. F. El-Kady, Y. Shao and R. B. Kaner, *Nat. Rev. Mater.*, 2016, **1**, 16033.
6 A. Manthiram, Y. Fu, S. H. Chung, C. Zu and Y. S. Su, *Chem. Rev.*, 2014, **114**, 11751–11787.
7 J. B. Goodenough, *Acc. Chem. Res.*, 2013, **46**, 1053–1061.
8 X. Xu, C. Niu, M. Duan, X. Wang, L. Huang, J. Wang, L. Pu, W. Ren, C. Shi and J. Meng, *Nat. Commun.*, 2017, **8**, 460–470.
9 X. Wang, X. Xu, C. Niu, J. Meng, M. Huang, X. Liu, Z. Liu and L. Mai, *Nano Lett.*, 2017, **17**, 544–550.
10 W. Ren, M. Qin, Z. Zhu, M. Yan, Q. Li, L. Zhang, D. Liu and L. Mai, *Nano Lett.*, 2017, **17**, 4713–4718.
11 K. A. Owusu, L. Qu, J. Li, Z. Wang, K. Zhao, C. Yang, K. M. Hercule, C. Lin, C. Shi, Q. Wei, L. Zhou and L. Mai, *Nat. Commun.*, 2017, **8**, 14264.
12 P. G. Bruce, S. A. Freunberger, L. J. Hardwick and J. M. Tarascon, *Nat. Mater.*, 2012, **11**, 19–29.
13 X. Ji, K. T. Lee and L. F. Nazar, *Nat. Mater.*, 2009, **8**, 500–506.
14 J. Lu, L. Li, J.-B. Park, Y.-K. Sun, F. Wu and K. Amine, *Chem. Rev.*, 2014, **114**, 5611–5640.
15 Y. Yang, G. Zheng and Y. Cui, *Chem. Soc. Rev.*, 2013, **42**, 3018–3032.
16 Z. W. Seh, Y. Sun, Q. Zhang and Y. Cui, *Chem. Soc. Rev.*, 2016, **45**, 5605–5634.
17 Z. Wang, Y. Dong, H. Li, Z. Zhao, H. B. Wu, C. Hao, S. Liu, J. Qiu and X. W. Lou, *Nat. Commun.*, 2014, **5**, 5002.
18 R. Xu, J. Lu and K. Amine, *Adv. Energy Mater.*, 2015, **5**, 1500408.
19 A. Manthiram, Y. Fu, S.-H. Chung, C. Zu and Y.-S. Su, *Chem. Rev.*, 2014, **114**, 11751–11787.
20 M. Wild, L. O'Neill, T. Zhang, R. Purkayastha, G. Minton, M. Marinescu and G. J. Offer, *Energy Environ. Sci.*, 2015, **8**, 3477–3494.

21 Y.-X. Yin, S. Xin, Y.-G. Guo and L.-J. Wan, *Angew. Chem., Int. Ed.*, 2013, **52**, 13186–13200.
22 X. Liu, J. Q. Huang, Q. Zhang and L. Mai, *Adv. Mater.*, 2017, **29**, 1601759.
23 C. Lin, C. Niu, X. Xu, K. Li, Z. Cai, Y. Zhang, X. Wang, L. Qu, Y. Xu and L. Mai, *Phys. Chem. Chem. Phys.*, 2016, **18**, 22146–22153.
24 B. Papandrea, X. Xu, Y. Xu, C.-Y. Chen, Z. Lin, G. Wang, Y. Luo, M. Liu, Y. Huang, L. Mai and X. Duan, *Nano Res.*, 2016, **9**, 240–248.
25 J. Hassoun and B. Scrosati, *Angew. Chem., Int. Ed.*, 2010, **49**, 2371–2374.
26 K. Cai, M. K. Song, E. J. Cairns and Y. Zhang, *Nano Lett.*, 2012, **12**, 6474–6479.
27 J. Guo, Z. Yang, Y. Yu, H. D. Abruña and L. A. Archer, *J. Am. Chem. Soc.*, 2013, **135**, 763–767.
28 C. Nan, L. Zhan, H. Liao, M. K. Song, Y. Li and E. J. Cairns, *J. Am. Chem. Soc.*, 2014, **136**, 4659–4663.
29 W. S. Zhi, H. Wang, P. C. Hsu, Q. Zhang, W. Li, G. Zheng, H. Yao and Y. Cui, *Energy Environ. Sci.*, 2014, **7**, 672–676.
30 Y. Fu, C. Zu and A. Manthiram, *J. Am. Chem. Soc.*, 2013, **135**, 18044–18047.
31 Y. Yang, G. Zheng, S. Misra, J. Nelson, M. F. Toney and Y. Cui, *J. Am. Chem. Soc.*, 2012, **134**, 15387–15394.
32 F. Wu, H. Kim, A. Magasinski, J. T. Lee, H. T. Lin and G. Yushin, *Adv. Energy Mater.*, 2014, **4**, 1220–1225.
33 Z. Lin, Z. Liu, N. J. Dudney and C. Liang, *ACS Nano*, 2013, **7**, 2829–2833.
34 S. Evers and L. F. Nazar, *Acc. Chem. Res.*, 2013, **46**, 1135–1143.
35 L. Ma, K. E. Hendrickson, S. Wei and L. A. Archer, *Nano Today*, 2015, **10**, 315–338.
36 Y. V. Mikhaylik and J. R. Akridge, *J. Electrochem. Soc.*, 2004, **151**, A1969–A1976.
37 C. Barchasz, F. Molton, C. Duboc, J.-C. Lepretre, S. Patoux and F. Alloin, *Anal. Chem.*, 2012, **84**, 3973–3980.
38 L. Mai, M. Yan and Y. Zhao, *Nature*, 2017, **546**, 469–470.
39 G. Zhang, T. Xiong, L. He, M. Yan, K. Zhao, X. Xu and L. Mai, *J. Mater. Sci.*, 2017, **52**, 3697–3718.
40 A. G. Gurlo and R. Riedel, *Angew. Chem., Int. Ed.*, 2007, **46**, 3826–3848.
41 J. Conder, R. Bouchet, S. Trabesinger, C. Marino, L. Gubler and C. Villevieille, *Nat. Energy*, 2017, **2**, 17069.
42 J. Kulisch, H. Sommer, T. Brezesinski and J. Janek, *Phys. Chem. Chem. Phys.*, 2014, **16**, 18765–18771.
43 J. Nelson, S. Misra, Y. Yang, A. Jackson, Y. Liu, H. Wang, H. Dai, J. C. Andrews, Y. Cui and M. F. Toney, *J. Am. Chem. Soc.*, 2012, **134**, 6337–6343.
44 A. Schneider, C. Weidmann, C. Suchomski, H. Sommer, J. Janek and T. Brezesinski, *Chem. Mater.*, 2015, **27**, 1674–1683.
45 M. Lowe, J. Gao and H. Abruna, *RSC Adv.*, 2014, **4**, 18347–18353.
46 W. Zhu, A. Paolella, C.-S. Kim, D. Liu, Z. Feng, C. Gagnon, J. Trottier, A. Vijh, A. Guerfi and A. Mauger, *Sustainable Energy Fuels*, 2017, **1**, 737–747.
47 R. Demircakan, M. Morcrette, G. Babu, A. Guéguen, R. Dedryvère and J. M. Tarascon, *Energy Environ. Sci.*, 2013, **6**, 176–182.
48 C. Villevieille and P. Novák, *J. Mater. Chem. A*, 2013, **1**, 13089–13092.
49 S. Waluś, C. Barchasz, R. Bouchet, J.-C. Leprêtre, J.-F. Colin, J.-F. Martin, E. Elkam, C. Baehtz and F. Alloin, *Adv. Energy Mater.*, 2015, **5**, 1500165.
50 S. Walus, C. Barchasz, J.-F. Colin, J.-F. Martin, E. Elkaim, J.-C. Lepretre and F. Alloin, *Chem. Commun.*, 2013, **49**, 7899–7901.
51 N. A. Cañas, S. Wolf, N. Wagner and K. A. Friedrich, *J. Power Sources*, 2013, **226**, 313–319.
52 A. Paolella, W. Zhu, H. Marceau, C. S. Kim, Z. Feng, D. Liu, C. Gagnon, J. Trottier, G. Abdelbast and P. Hovington, *J. Power Sources*, 2016, **325**, 641–645.
53 S. Waluś, C. Barchasz, R. Bouchet, J. C. Leprêtre, J. F. Colin, J. F. Martin, E. Elkaïm, C. Baehtz and F. Alloin, *Adv. Energy Mater.*, 2015, **5**, 1500165.
54 H. S. Ryu, H. J. Ahn, K. W. Kim, J. H. Ahn and J. Y. Lee, *J. Power Sources*, 2006, **153**, 360–364.
55 S. S. Jeong, Y. T. Lim, Y. J. Choi, G. B. Cho, K. W. Kim, H. J. Ahn and K. K. Cho, *J. Power Sources*, 2007, **174**, 745–750.
56 L. Yuan, X. Qiu, L. Chen and W. Zhu, *J. Power Sources*, 2009, **189**, 127–132.
57 X. Ji, S. Evers, R. Black and L. F. Nazar, *Nat. Commun.*, 2011, **2**, 325.
58 J. M. Yuk, J. Park, P. Ercius, K. Kim, D. J. Hellebusch, M. F. Crommie, J. Y. Lee, A. Zettl and A. P. Alivisatos, *Science*, 2012, **336**, 61–64.
59 J. Zhao, Q. Deng, S. M. Avdoshenko, L. Fu, J. Eckert and M. H. Rummeli, *Proc. Natl. Acad. Sci. U. S. A.*, 2014, **111**, 15641–15646.
60 J. Y. Huang, L. Zhong, C. M. Wang, J. P. Sullivan, W. Xu, L. Q. Zhang, S. X. Mao, N. S. Hudak, X. H. Liu, A. Subramanian, H. Y. Fan, L. A. Qi, A. Kushima and J. Li, *Science*, 2010, **330**, 1515–1520.
61 W. Tang, Z. Chen, B. Tian, H. W. Lee, X. Zhao, X. Fan, Y. Fan, K. Leng, C. Peng and M. H. Kim, *J. Am. Chem. Soc.*, 2017, **139**, 10133–10141.
62 H. Kim, J. T. Lee, A. Magasinski, K. Zhao, Y. Liu and G. Yushin, *Adv. Energy Mater.*, 2015, **5**, 1501306.
63 Z. L. Xu, J. Q. Huang, W. G. Chong, X. Qin, X. Wang, L. Zhou and J. K. Kim, *Adv. Energy Mater.*, 2017, **7**, 1602078.
64 J. Zhao, Q. Deng, S. M. Avdoshenko, L. Fu, J. Eckert and M. H. Rummeli, *Proc. Natl. Acad. Sci. U. S. A.*, 2014, **111**, 15641–15646.
65 J. Y. Huang, L. Zhong, C. M. Wang, J. P. Sullivan, W. Xu, L. Q. Zhang, S. X. Mao, N. S. Hudak, X. H. Liu and A. Subramanian, *Science*, 2010, **330**, 1515–1520.
66 X. H. Liu, J. W. Wang, S. Huang, F. F. Fan, X. Huang, Y. Liu, S. Krylyuk, J. Yoo, S. A. Dayeh, A. V. Davydov, S. X. Mao, S. T. Picraux, S. L. Zhang, J. Li, T. Zhu and J. Y. Huang, *Nat. Nanotechnol.*, 2012, **7**, 749–756.

67 F. Wang, H.-C. Yu, M.-H. Chen, L. Wu, N. Pereira, K. Thornton, A. V. d. Ven, Y. Zhu, G. G. Amatucci and J. Graetz, *Nat. Commun.*, 2012, **3**, 1201.
68 Z. Wang, D. Santhanagopalan, W. Zhang, F. Wang, H. L. Xin, K. He, J. Li, N. Dudney and Y. S. Meng, *Nano Lett.*, 2016, **16**, 3760–3767.
69 J. Nelson Weker and M. F. Toney, *Adv. Funct. Mater.*, 2015, **25**, 1622–1637.
70 S. Y. Lang, Y. Shi, Y. G. Guo, D. Wang, R. Wen and L. J. Wan, *Angew. Chem., Int. Ed.*, 2016, **51**, 15835–15839.
71 S. C. Chao, Y. C. Yen, Y. F. Song, Y. M. Chen, H. C. Wu and N. L. Wu, *Electrochem. Commun.*, 2010, **12**, 234–237.
72 R. Falcone, C. Jacobsen, J. Kirz, S. Marchesini, D. Shapiro and J. Spence, *Contemp. Phys.*, 2011, **52**, 293–318.
73 C.-N. Lin, W.-C. Chen, Y.-F. Song, C.-C. Wang, L.-D. Tsai and N.-L. Wu, *J. Power Sources*, 2014, **263**, 98–103.
74 H. Marceau, C. S. Kim, A. Paolella, S. Ladouceur, M. Lagacé, M. Chaker, A. Vijh, A. Guerfi, C. M. Julien, A. Mauger, M. Armand, P. Hovington and K. Zaghib, *J. Power Sources*, 2016, **319**, 247–254.
75 G. R. Y. Qiu, J. Yang, G. Li, S. Ma, X. Wang, Z. Pan, Y. Hou, M. Liu, F. Ye, W. Li, Z. W. Seh, X. Tao, H. Yao, N. Liu, R. Zhang, G. Zhou, J. Wang, S. Fan, Y. Cui and Y. Zhang, *Adv. Energy Mater.*, 2015, **5**, 1501369–1501377.
76 K. J. Harry, D. T. Hallinan, D. Y. Parkinson, A. A. Macdowell and N. P. Balsara, *Nat. Mater.*, 2014, **13**, 69–73.
77 M. Ebner, F. Geldmacher, F. Marone, M. Stampanoni and V. Wood, *Adv. Energy Mater.*, 2013, **3**, 845–850.
78 L. Zielke, T. Hutzenlaub, D. R. Wheeler, I. Manke, T. Arlt, N. Paust, R. Zengerle and S. Thiele, *Adv. Energy Mater.*, 2014, **4**, 1301617.
79 S. K. Babu, A. I. Mohamed, J. F. Whitacre and S. Litster, *J. Power Sources*, 2015, **283**, 314–319.
80 V. Yufit, P. Shearing, R. W. Hamilton, P. D. Lee, M. Wu and N. P. Brandon, *Electrochem. Commun.*, 2011, **13**, 608–610.
81 M. Ebner, F. Marone, M. Stampanoni and V. Wood, *Science*, 2013, **342**, 716–720.
82 A. Yermukhambetova, C. Tan, S. R. Daemi, Z. Bakenov, J. A. Darr, D. J. L. Brett and P. R. Shearing, *Sci. Rep.*, 2016, **6**, 35291–35299.
83 Y. Sun, W. S. Zhi, W. Li, H. Yao, G. Zheng and Y. Cui, *Nano Energy*, 2015, **11**, 579–586.
84 Y. Gorlin, A. Siebel, M. Piana, T. Huthwelker, H. Jha, G. Monsch, F. Kraus, H. A. Gasteiger and M. Tromp, *J. Electrochem. Soc.*, 2015, **162**, A1146–A1155.
85 J. Gao, M. A. Lowe, Y. Kiya and H. D. Abruña, *J. Phys. Chem. C*, 2011, **115**, 25132–25137.
86 M. Cuisinier, P. E. Cabelguen, S. Evers, G. He, M. Kolbeck, A. Garsuch, T. Bolin, M. Balasubramanian and L. F. Nazar, *J. Phys. Chem. Lett.*, 2013, **4**, 3227–3232.
87 K. H. Wujcik, T. A. Pascal, C. D. Pemmaraju, D. Devaux, W. C. Stolte, N. P. Balsara and D. Prendergast, *Adv. Energy Mater.*, 2015, **5**, 1500285.
88 T. A. Pascal, K. H. Wujcik, J. Velasco-Velez, C. H. Wu, A. A. Teran, M. Kapilashrami, J. Cabana, J. H. Guo, M. Salmeron, N. Balsara and D. Prendergast, *J. Phys. Chem. Lett.*, 2014, **5**, 1547.
89 M. A. Lowe and J. Gao, *RSC Adv.*, 2014, **4**, 18347–18353.
90 K. H. Wujcik, J. Velasco-Velez, C. H. Wu, T. Pascal, A. A. Teran, M. A. Marcus, J. Cabana, J. Guo, D. Prendergast, M. Salmeron and N. P. Balsara, *J. Electrochem. Soc.*, 2014, **161**, A1100–A1106.
91 M. Cuisinier, P. E. Cabelguen, B. D. Adams, A. Garsuch, M. Balasubramanian and L. F. Nazar, *Energy Environ. Sci.*, 2014, **7**, 2697–2705.
92 R. Dominko, M. U. Patel, V. Lapornik, A. Vizintin, M. Koželj, N. a. N. Tušar, I. Arčon, L. Stievano and G. Aquilanti, *J. Phys. Chem. C*, 2015, **119**, 19001–19010.
93 P. Zhu, J. Song, D. Lv, D. Wang, C. Jaye, D. A. Fischer, T. Wu and Y. Chen, *J. Phys. Chem. C*, 2014, **118**, 7765–7771.
94 M. Cuisinier, C. Hart, M. Balasubramanian, A. Garsuch and L. F. Nazar, *Adv. Energy Mater.*, 2015, **5**, 1–6.
95 D. Zheng, D. Liu, J. B. Harris, T. Ding, J. Si, S. Andrew, D. Qu, X. Q. Yang and D. Qu, *ACS Appl. Mater. Interfaces*, 2016, **9**, 4326–4332.
96 M. Vijayakumar, N. Govind, E. Walter, S. D. Burton, A. Shukla, A. Devaraj, J. Xiao, J. Liu, C. Wang and A. Karim, *Phys. Chem. Chem. Phys.*, 2014, **16**, 10923–10932.
97 M. U. M. Patel, I. Arčon, G. Aquilanti, L. Stievano, G. Mali and R. Dominko, *ChemPhysChem*, 2014, **15**, 894–904.
98 J. Hannauer, J. Scheers, J. Fullenwarth, B. Fraisse, L. Stievano and P. Johansson, *ChemPhysChem*, 2015, **16**, 2755–2759.
99 H. L. Wu, L. A. Huff and A. A. Gewirth, *ACS Appl. Mater. Interfaces*, 2015, **7**, 1709–1719.
100 J.-J. Chen, R. Yuan, J.-M. Feng, Q. Zhang, J.-X. Huang, G. Fu, M. Zheng, B. Ren and Q.-F. Dong, *Chem. Mater.*, 2015, **27**, 2048–2055.
101 M. Hagen, P. Schiffels, M. Hammer, S. Dörfler, J. Tübke, M. J. Hoffmann, H. Althues and S. Kaskel, *J. Electrochem. Soc.*, 2013, **160**, A1205–A1214.
102 Q. Zhao, X. Hu, K. Zhang, N. Zhang, Y. Hu and J. Chen, *Nano Lett.*, 2015, **15**, 721–726.
103 W. Zhu, A. Paolella, C.-S. Kim, D. Liu, Z. Feng, C. Gagnon, J. Trottier, A. Vijh, A. Guerfi and A. Mauger, *Sustainable Energy Fuels*, 2017, **1**, 737–747.
104 Y. Diao, K. Xie, S. Xiong and X. Hong, *J. Electrochem. Soc.*, 2012, **159**, A421–A425.
105 J.-T. Yeon, J.-Y. Jang, J.-G. Han, J. Cho, K. T. Lee and N.-S. Choi, *J. Electrochem. Soc.*, 2012, **159**, A1308–A1314.
106 H.-L. Wu, L. A. Huff and A. A. Gewirth, *ACS Appl. Mater. Interfaces*, 2015, **7**, 1709–1719.
107 J. Hannauer, J. Scheers, J. Fullenwarth, B. Fraisse, L. Stievano and P. Johansson, *ChemPhysChem*, 2015, **16**, 2755–2759.
108 J. J. Chen, R. M. Yuan, J. M. Feng, Q. Zhang, J. X. Huang, G. Fu, M. S. Zheng, B. Ren and Q. F. Dong, *Chem. Mater.*, 2015, **27**, 2048–2055.

109 J. Hannauer, J. Scheers, J. Fullenwarth, B. Fraisse, L. Stievano and P. Johansson, *ChemPhysChem*, 2015, **16**, 2705–2705.
110 H. Marceau, C. S. Kim, A. Paolella, S. Ladouceur, M. Lagacé, M. Chaker, A. Vijh, A. Guerfi, C. M. Julien, A. Mauger, M. Armand, P. Hovington and K. Zaghib, *J. Power Sources*, 2016, **319**, 247–254.
111 M. U. Patel, R. Demir-Cakan, M. Morcrette, J. M. Tarascon, M. Gaberscek and R. Dominko, *ChemSusChem*, 2013, **6**, 1177–1181.
112 M. U. M. Patel and R. Dominko, *ChemSusChem*, 2014, **7**, 2167–2175.
113 N. A. Cañas, D. N. Fronczek, N. Wagner, A. Latz and K. A. Friedrich, *J. Phys. Chem. C*, 2014, **118**, 12106–12114.
114 C. Barchasz, F. Molton, C. Duboc, J.-C. Leprêtre, S. Patoux and F. Alloin, *Anal. Chem.*, 2012, **84**, 3973–3980.
115 A. Kawase, S. Shirai, Y. Yamoto, R. Arakawa and T. Takata, *Phys. Chem. Chem. Phys.*, 2014, **16**, 9344–9350.
116 N. Xu, T. Qian, X. Liu, J. Liu, Y. Chen and C. Yan, *Nano Lett.*, 2017, **17**, 538–543.
117 Q. Zou and Y. C. Lu, *J. Phys. Chem. Lett.*, 2016, **7**, 1518.
118 J. Liu, T. Qian, M. Wang, X. Liu, N. Xu, Y. You and C. Yan, *Nano Lett.*, 2017, **17**, 5064–5070.
119 J. Zhou, T. Qian, N. Xu, M. Wang, X. Ni, X. Liu, X. Shen and C. Yan, *Adv. Mater.*, 2017, **29**, 1605160.
120 C. Barchasz, F. Molton, C. Duboc, J. C. Leprêtre, S. Patoux, F. Alloin and A. Chem, *Anal. Chem.*, 2012, **84**, 3973–3980.
121 N. Xu, T. Qian, X. Liu, J. Liu, Y. Chen and C. Yan, *Nano Lett.*, 2017, **17**, 538–543.
122 M. U. M. Patel and R. Dominko, *ChemSusChem*, 2014, **7**, 2167.
123 H. Marceau, A. Paolella, S. Ladouceur, M. Lagacé, M. Chaker, A. Vijh, A. Guerfi, C. M. Julien, A. Mauger, M. Armand, P. Hovington and K. Zaghib, *J. Power Sources*, 2016, **319**, 247–254.
124 B. Key, R. Bhattacharyya, M. Morcrette, V. Seznec, J. M. Tarascon and C. P. Grey, *J. Am. Chem. Soc.*, 2009, **131**, 9239–9249.
125 R. Bhattacharyya, B. Key, H. Chen, A. S. Best, A. F. Hollenkamp and C. P. Grey, *Nat. Mater.*, 2010, **9**, 504–510.
126 L. A. Huff, J. L. Rapp, J. A. Baughman, P. L. Rinaldi and A. A. Gewirth, *Surf. Sci.*, 2015, **631**, 295–300.
127 K. A. See, L. Michal, J. M. Griffin, B. Sylvia, P. D. Matthews, E. Alexandra, V. D. V. Anton, D. S. Wright, A. J. Morris and C. P. Grey, *J. Am. Chem. Soc.*, 2014, **136**, 16368–16377.
128 M. U. Patel, I. Arčon, G. Aquilanti, L. Stievano, G. Mali and R. Dominko, *ChemPhysChem*, 2014, **15**, 894–904.
129 J. Xiao, J. Z. Hu, H. Chen, M. Vijayakumar, J. Zheng, H. Pan, E. D. Walter, M. Hu, X. Deng, J. Feng, B. Y. Liaw, M. Gu, Z. D. Deng, D. Lu, S. Xu, C. Wang and J. Liu, *Nano Lett.*, 2015, **15**, 3309–3316.
130 K. A. See, M. Leskes, J. M. Griffin, S. Britto, P. D. Matthews, A. Emly, A. V. d. Ven, D. S. Wright, A. J. Morris, C. P. Grey and R. Seshadri, *J. Am. Chem. Soc.*, 2014, **136**, 16368–16377.
131 H. Wang, N. Sa, M. He, X. Liang, L. F. Nazar, M. Balasubramanian, K. G. Gallagher and B. Key, *J. Phys. Chem. C*, 2017, **364**, 266–271.
132 D. Zheng, D. Qu, X. Q. Yang, X. Yu, H. S. Lee and D. Qu, *Adv. Energy Mater.*, 2015, **5**, 1401888.
133 D. Zheng, X. Zhang, J. Wang, D. Qu, X. Yang and D. Qu, *J. Power Sources*, 2016, **301**, 312–316.
134 D. Zheng, X. Zhang, C. Li, M. E. Mckinnon, R. G. Sadok, D. Qu, X. Yu, H. S. Lee and X. Q. Yang, *J. Electrochem. Soc.*, 2015, **162**, A203–A206.
135 D. Zheng and D. Qu, *J. Electrochem. Soc.*, 2014, **161**, A1164–A1166.
136 S. Risse, C. J. Jafta, Y. Yang, N. Kardjilov, A. Hilger, I. Manke and M. Ballauff, *Phys. Chem. Chem. Phys.*, 2016, **18**, 10630–10636.
137 Y. Yang, S. Risse, S. Mei, C. J. Jafta, Y. Lu, C. Stöcklein, N. Kardjilov, I. Manke, J. Gong and Z. Kochovski, *Energy Storage Mater.*, 2017, **9**, 96–104.
138 M. I. Nandasiri, L. E. Camacho-Forero, A. M. Schwarz, V. Shutthanandan, S. Thevuthasan, P. B. Balbuena, K. T. Mueller and V. Murugesan, *Chem. Mater.*, 2017, **29**, 4728–4737.
139 Y. U. Paulechka, D. H. Zaitsau, G. J. Kabo and A. A. Strechan, *Thermochim. Acta*, 2005, **439**, 158–160.
140 J. Zheng, M. Gu, H. Chen, P. Meduri, M. Engelhard, J. G. Zhang, J. Liu and J. Xiao, *J. Mater. Chem. A*, 2013, **1**, 8464–8470.
141 Q. Wang, Z. Jianming, E. Wailter, P. Huilin, L. Lv, P. Zuo, H. Chen, Z. D. Deng, B. Y. Liaw, X. Yu, X. Yang, J. G. Zhang, J. Li and J. Xiao, *J. Electrochem. Soc.*, 2015, **162**, A474–A478.
142 X. Yu, H. Pan, Y. Zhou, P. Northrup, J. Xiao, S. Bak, M. Liu, K. W. Nam, D. Qu, J. Liu, T. Wu and X. Yang, *Adv. Energy Mater.*, 2015, **5**, 1500072.

